# Asian Summer Monsoon Anticyclone: Trends and Variability

Ghouse Basha[1], M. Venkat Ratnam[1] and Pangaluru Kishore[2]
[1]National Atmospheric Research Laboratory, Department of Space, Gadanki-517112, India.

[2] Department of Earth System Science, University of California, Irvine, CA, 92697, USA.

Correspondence to: Ghouse Basha (mdbasha@narl.gov.in)

**Abstract**

The Asian Summer Monsoon Anticyclone (ASMA) has been a topic of intensive research in recent times through its variability in dynamics, chemistry and radiation. This work explores the spatial variability and the trends of the ASMA using observational and reanalysis data sets. Our analysis indicates that the spatial extent and magnitude of ASMA is greater during July and August compared to June and September. The decadal variability of the anticyclone is very large at the edges of the anticyclone than at the core region. Significant decadal variability is observed in the northeast and southwest parts of ASMA with reference to the 1951-1960 period. The strength of the ASMA shows a drastic increase in zonal wind anomalies in terms of temporal variation. Further, our results show that the extent of the anticyclone is greater during the active phase of the monsoon, strong monsoon years, and La Niña events. Significant warming with strong westerlies is observed exactly over the Tibetan Plateau from the surface to tropopause during the active phase of the monsoon, strong monsoon years, and during La Niña events. Our results support the transport process over Tibetan Plateau and the Indian region during active, strong monsoon years and during strong La Niña years. It is suggested to consider different phases of monsoon while interpreting the variability of pollutants/trace gases in the anticyclone.

*Keywords*: Asian Monsoon, anticyclone, geopotential height, La Niño, El Niño, and rainfall.

## 1. Introduction

The Asian Summer Monsoon Anticyclone (ASMA) is a dominant circulation in the Northern Hemisphere (NH) summer in the Upper Troposphere and Lower Stratosphere (UTLS), which extends from Asia to the Middle East. ASMA is bordered by the subtropical westerly jet in the north and easterly jets to the south. The Asian Summer Monsoon (ASM) dynamics act as a pathway for the transport of trace gases and pollutants both vertically (through convection) and horizontally (through low-level jet and tropical easterly jet). The ASMA circulation responds to heating corresponding to the deep convection of the south Asian monsoon (Hoskins and Rodwell, 1995; Highwood and Hoskins, 1998). This strong anticyclone circulation isolates the air and is tied to the outflow of deep convection, which has distinct maximum characteristics in terms of dynamical and chemical variability (Randel and Park, 2006; Park et al., 2007). Recently, the anticyclone circulation in UTLS has been paid more attention by researchers in order to understand the dynamics, chemistry, and radiation of the region. This problem has been discussed by several authors (e.g., Park et al., 2007; Fadnavis et al., 2014; Glatthor et al., 2015; Vernier et al., 2015; Santee et al., 2017). Deep convection during monsoon can transport tropospheric tracers from the surface to the UTLS (Vogel et al., 2015; Tissier and Legras, 2016). The tracers which are transported are confined in the anticyclone will affect the trace gas concentration in the UTLS resulting in significant changes in radiative forcings (Solomon et al., 2010; Riese et al., 2012; Hossaini et al., 2015). The center of the anticyclone is located either over the Iranian Plateau or over the Tibetan Plateau where the distribution of pollutants and tracers vary significantly (Yan et al., 2011).

The spatial extent, strength, and the location of an anticyclone vary on several temporal scales caused by internal dynamical variability of the Asian monsoon (Zhang et al., 2002; Randel and Park, 2006; Garny and Randel, 2013; Vogel et al., 2015; Pan et al., 2016).

However, the variability of the anticyclone structure and response to Indian monsoon activity are not understood. Further, the tracers (O3, and CO etc.,) trapped in the anticyclone during the same period in the UTLS region. Since the anticyclone extends from the Middle East to East Asia, trapped pollutants are expected to make a large radiative forcing to the background atmosphere. Thus, it is essential to understand the variability of anticyclone structure itself in detail and its response to Indian Summer Monsoon (ISM). Therefore, in the first part of the study, we investigate the spatial, inter-annual and decadal variations of the anticyclone. Since the Indian monsoon responds at different time scales, we also investigated the anticyclone variability with respect to the active and break spells of the Indian monsoon, strong and weak monsoon years, and the stronger El Nino Southern Oscillation (ENSO) years. For this, we have utilized the NCEP/NCAR reanalysis geopotential height from 1951 to 2016. The structure of the paper is as follows. We describe the data sets used in this study in Section 2. Section 3 contains the seasonal and decadal variation of the anticyclone. Section 4 shows the influence of ISM on anticyclone i.e. active and break spells, strong and weak monsoon years, and ENSO's effects on the anticyclone. Finally, we discuss our results presented in Section 5.

## 2. Data and Methodology

### 2.1. NCEP/NCAR Reanalysis

The National Center for Environmental Prediction (NCEP), in collaboration with the National Center for Atmospheric Research (NCAR) produces reanalysis data from a consistent assimilation and modeling procedure that incorporates all the available observed conditions obtained from conventional and satellite information from 1951 to the present (Kalnay et al. 1996). We used NCEP/NCAR reanalysis daily geopotential height (GPH) and wind data from the years 1951 to 2016. The NCEP/NCAR data assimilation uses a 3D-variational analysis scheme with 28 pressure levels and triangular truncation of 62 waves (horizontal resolution of 200m). Both GPH and temperature at the chosen standard levels are described as class output variables (Kalnay et al. 1996) i.e. they are strongly influenced by observed data. Only the Indian summer monsoon months (June, July, and August, September) containing gridded daily data were considered in this study. The NCEP/NCAR reanalysis data had a spatial resolution of 2.5$^{o}$. The seasonal values are estimated from daily data. To identify the spatial and temporal variations of the anticyclone center, we used the monthly mean values of the GPH and the zonal wind component. The quality of NCEP GPH reanalysis data can be found from Bromwich et al. (2007).

### 2.2. IMD Gridded Precipitation Data

The India Meteorological Department (IMD) high-resolution (0.25$^{o}$x0.25$^{o}$) gridded precipitation data is used to identify the active and break spells during June, July and August months from 1951-2016. This precipitation data has been validated extensively with observational and reanalysis data sets and displays a very good correlation (Kishore et al., 2016). For identification of active (or wet) and break (or dry) spells, we followed a similar procedure as described by Rajeevan et al. (2010) and Pai et al. (2016) over the monsoon core zone (18$^{o}$N-28$^{o}$N, and 65$^{o}$E-88$^{o}$E). Data from 1951-2016 have been used.

### 2.3. GNSS Radio Occultation (RO) Data

We have also used the Global Navigation Satellite System (GNSS) Radio Occultation (RO) data for investigating the temperature anomaly. The basic measurement principle of RO exploits the atmosphere-induced phase delay in the GNSS signals, which are recorded in the low earth-orbiting satellite. This technique provides vertical profiles of refractivity, density, pressure, temperature, and water vapor (Kursinski et al., 1997). The temperature profiles from this technique are available with low horizontal (~200-300 km) and high vertical resolutions (10-35 km) with an accuracy of <0.5 K. We used the CHAllenging Minisatellite Payload (CHAMP) and Constellation Observing System for Meteorology, Ionosphere, and Climate (COSMIC) covering the period from 2002 to 2016.

The CHAMP satellite was launched on 15 July 2000 into a circular orbit by Germany to measure the Earth's gravity and magnetic field and to provide global RO soundings (Wickert et al. 2001). About ~230 RO profiles per day were measured by the CHAMP payload since 2002. The CHAMP payload was solely designed to track the setting occultations, and the RO event gets terminated when the signal is lost, which results in a decrease in the number of occultations with a decreasing altitude (Beyerle et al. 2006). This receiver measures the phase delay of radio wave signals that are occulted by the Earth's atmosphere. From this phase delay, it is possible to retrieve the bending angle and refractivity vertical profiles.

COSMIC consists of a constellation of 6 satellites, which was launched in April 2006 to a circular, 72° inclination orbit at a 512 km altitude capable of receiving signals from the Global Positioning System (GPS) (Anthes et al., 2008). Compared to previous satellites, COSMIC satellites employed an open loop mode, which can track both the rising and setting of occultations (Schreiner et al. 2007). The open-loop tracking technique significantly reduces the GPS RO inversion biases by eliminating tracking errors (Sokolovskiy et al. 2006). The COSMIC temperature profiles display a very good agreement with radiosonde data, reanalyses, and models (Rao et al., 2009; Kishore et al., 2011; Kishore et al., 2016). The CHAMP and COSMIC GPSRO data was interpolated to 200 m from their native resolution. We derived the cold point tropopause altitude/temperature over the ASMA region as discussed by Ratnam et al. (2014) and Ravindrababu et al. (2015). Both the CHAMP and COSMIC data were obtained from COSMIC Data Analysis and Archive Center (CDAAC) (https://cdaac-www.cosmic.ucar.edu/cdaac/products.html).

## 3. Results and Discussion

### 3.1. Variability of the Anticyclone

The climatological spatial variability of the GPH and wind vectors at 100 hPa during June, July, August and September months from NCEP reanalysis data is shown in Figure 1(a, b, c & d). The anticyclone circulation is clearly depicted during June, July, August, and September by wind vectors (Figure 1). During the month of September and June, the values of GPH are low compared to July and August which represents the spatial extent of the anticyclone. The spatial extent and intensity of the anticyclone are greater during July compared to the other months. During July and August, the anticyclone extends from East Asia to the Middle East. The spatial extent of the anticyclone circulation is clearly evident in the grid 15$^{o}$N-45$^{o}$N; 30$^{o}$E-120$^{o}$E at 100 hPa level and the climatological averaged values of GPH varies from 16.5-17 km in NCEP reanalysis during 1951-2016. Using the modified potential vorticity equation, Randel et al. (2006) showed the spatial variation of the anticyclone where GPH values are stationary in the range of 16.75-16.9 km. Similarly, Park et al. (2007) showed the anticyclone structure from the strongest wind at 100 hPa through streamline function. Bian et al. (2012) reported the spatial variability of the anticyclone using 16.77 km and 16.90 km in the GPH contour as the lower and the upper boundary, respectively. Thus, these empirically selected GPH values represent the anticyclone boundaries. Therefore, in this present study, we have chosen the values from 16.75 to 16.9 km to investigate the spatial features of the anticyclone and the resultant picture is depicted in Figure 1(e, f, g & h). The spatial extent and existence of the anticyclone are highly prominent during July and August compared to June. During the September month, very low values of GPH are seen compared to July and August. Therefore, we considered the average of July and August GPH from 1951-2016 for further analysis as shown in Figure S1. The core region and the spatial extent of the anticyclone are clearly evident from Figure S1. The core region of the anticyclone shows bimodal distribution i.e. one core located at the south-western flank of the Himalayas and another over Iran. The core region over the south-western flank of

Himalayas is due to large scale updraft, which is caused by the moist energy over Indo-Gangetic plain, heating of Tibetan plateau, and the orographic forcing of the Himalayas. Severe heating over Arabian Peninsula supports the formation of the mid-tropospheric the anticyclone in the west. This anticyclone can merge intermittently within ASMA. It is also observed that the spatial extent of the anticyclone varies drastically at different temporal scales. Therefore, seasonal variation is much more pronounced.

The decadal variation of the anticyclone is studied with respect to the spatial variability. Figure 2 shows the decadal spatial variation of the anticyclone with reference to the years 1951-1960. The significant difference in the decadal variation is noticed in Figure 2. The edges (east, north, and west) of the anticyclone undergo drastic changes during the period 1961-1970. In case of 1971-1980 period, except for a small portion in the east, the whole anticyclone shows drastic changes. During the decade 1971-1980, the recorded GPH values in the anticyclone are lower by ~ 25 m when compared to the values in 1951-1960. This feature is quite opposite during 1981-1990 where high values (~30 m) are observed compared to those in the reference period. The GPH difference is significant over the west, northeast and southern regions of the anticyclone during the 1991-2000 period. Similar changes are observed during 2001-2010. Compared to all the decadal differences, 2011-2016 shows a completely different picture. The changes are only in the western and north-eastern corner, whereas other parts of the anticyclone do not show any change. From this analysis, we observed significant changes in the anticyclone even from one decade to another, which can result in a change in chemical and dynamical changes over this region.

Further, the spatial distribution of trend is estimated during the years 1951-2016 by using robust regression analysis at 95% confidence interval as displayed in Figure 3.. The edges on all sides of the anticyclone undergo noticeable changes compared to the core region. The east and north-west side of the anticyclone shows an increasing trend compared to other regions. The trends at the northern end are significant than the southern end. A few portions on the northern side of the anticyclone show a reduction in the strength. Therefore, in order to understand the asymmetry in the anticyclone variability, we have divided the anticyclone region into 4 different sectors as shown in Figure 4 based on the peak values of GPH along longitude and latitude cross-sections. The center values of GPH are located at 70°E longitude and 32.5°N Latitude. The four sectors can be divided into South-East (SE) (22.5°N-32.5°N), North-East (NE) (32.5°N-40°N) in the longitude band of 70°E-120°E, South-West (SW) (22.5°N-32.5°N), and North-West (NW) (32.5°N-40°N) at the 20°E-70°E longitude range. The area-averaged time series (July and August) of zonal wind anomalies in these sectors from 1951-2016 are shown in Figure 5. The zonal wind anomalies show a clearly increasing trend in all the sectors. From the year 1951 to 1980, the zonal wind anomalies are negative and shift to positive in all the sectors. The year 1980 represents the beginning of industrialization globally (Basha et al., 2017). The change is highly significant in the north-west and north-east sectors with a magnitude variability of 7.59 m/s from 1951-2016 whereas it is 5.44 m/s in the south-east and south-west sectors. In addition, we estimated the strength of the anticyclone during the monsoon season by using a difference in the zonal wind between the northern (30°N-40°N) and southern (10°N-20°N) flanks of the anticyclone, which is depicted in Figure 5e. A significant increase in the strength of the anticyclone is noticed from Figure 5e at a rate of 0.157 m/s per year (10.36 m/s from 1951-2016).

It is well known that the Indian monsoon rainfall varies at different time scales i.e. daily, sub-seasonal, interannual, decadal and centennial scales (Rajeevan et al., 2010). Precipitation during the monsoon varies from intra-seasonal scales between active (good rainfall) and break (less rainfall) spells. Any small change in the precipitation pattern will affect the anticyclone due to the thermodynamics involved in rainfall. In this study, we also investigated the anticyclone variability during the active and break spells of the Indian monsoon. The active and break spells were identified in July and August by using the high resolution gridded ($0.25^{o}$ x $0.25^{o}$) rainfall data from 1951 to 2016 as defined by Pai et al. (2010).

The number of active and break days is derived from the precipitation data shown in Figure S2 (a & b). Daily GPH, temperature, and zonal wind are taken from NCEP reanalysis whereas the tropopause altitude is derived from the GNSS RO data for active and break days. The anticyclone structure during active (red line) and break (blue line) days are shown in Figure 6a. Two interesting aspects of the anticyclone variability can be noticed between active and break days. One aspect is the extent of the anticyclone is large during active days compared to break days and another is the existence of two cell structures in the anticyclone core region during active days. The extent is large in the eastern and northern side in active days. The zonal (meridional) cross-section of temperature (color shade), zonal wind (contour lines) difference between active and break phase averaged in the longitude band of $80^{o}$E-$90^{o}$E (latitude band of $30^{o}$N-$40^{o}$N) along with cold point tropopause for active and break days is illustrated in Figures 6b & 6c. During active days, temperature shows cooling in tropical latitudes whereas it shows warming in the mid-latitudes from surface to the tropopause. Significant warming is observed during the active days in the mid-troposphere over the Tibetan Plateau and its northern side. Westerly (easterly) winds exist over the cooler (warmer) regions. The warm temperature anomalies stretch from 1.5 to 12 km in between $25^{o}$N and $60^{o}$N. The tropopause altitude is low (high) during the active (break) phase of Indian monsoon as shown in Figure 6b. The meridional cross-section of temperature anomalies displays significant warming from ~1.5 to 8 km over the Indian region. The tropopause altitude exemplifies random variability in the meridional cross-section.

As discussed previously, the anticyclone circulation is significant during the months of July and August when most of the precipitation occurs over India (Basha et al., 2013;

Basha et al., 2015; Kishore et al., 2015; Narendra Reddy et al., 2018). The influence of strong and weak monsoon years will have a drastic impact on anticyclone circulation. In order to understand these changes, we have divided the years into strong and weak monsoon years based on gridded precipitation data over the domain $5^{o}$N-$30^{o}$N and $70^{o}$E-$95^{o}$E from the years 1951-2016. This region is known to have heavy precipitation and orographic forcing, which helps transport of water vapor through deep convection to UTLS (Houze et al., 2007; Medina et al., 2010; Pan et al., 2016). The detrended precipitation represents the strong and weak monsoon years. Years with positive (negative) values of precipitation shows the strong (weak) monsoon years as shown in Figure S2b.The composite of mean distribution of the anticyclone circulation during strong and weak monsoon years is shown in Figure 7a based on GPH values at 100 hPa from NCEP reanalysis data. The circulation expands on the eastern and western sides of the anticyclone during the strong monsoon years (red line). The core of the anticyclone is significant during strong monsoon years. Clear eye structure is observed in the core of the anticyclone on left (right) during the strong (weak) monsoon years. The composite mean difference of temperature and zonal wind between the strong and weak monsoon years along with tropopause altitude averaged in the longitude range of 80-$85^{o}$E is shown in Figure 7b. The warmest temperature anomalies are observed over the Tibetan Plateau. Positive (warm) temperature anomalies exactly above the Tibetan Plateau (11 km) and negative (cooling) on both sides are noticed in the lower troposphere from Figure 7b. Strong easterlies (westerlies) winds are observed on the left (right) side of the Tibetan Plateau. The whole Tibetan Plateau acts as a barrier that drives the cold air to upper altitudes during strong monsoon years. Strong anticyclone circulation with strong westerlies at $35^{o}$N and easterlies on both sides with elevated tropopause represent the impacts of the strong monsoon vertically above the anticyclone. The rising motion over East Asia is excited by the local heating of the Tibetan Plateau links to the single stretch vertically. The longitude and altitude cross-section of temperature and wind anomalies shown in Figure 7c are averaged between a latitude band of 35-40$^{o}$N. Positive temperature anomalies are observed from the surface to 12 km in the longitudes 60-80$^{o}$E and stretch towards the west. This process clearly demonstrates that a large scale ascent develops over the Asian monsoon region. The tropopause altitude is high (low) during strong vertical motion and heavy precipitation is noticed over the region similar to that reported by Lau et al. (2018). The transport processes from the boundary layer to the tropopause occur on the east side of the anticyclone i.e. southern flank of Tibetan Plateau, northeast India and the head of the Bay of Bengal. This result is consistent with the previous studies by Bergman et al. (2013).

ENSO typically shows the strongest signal in boreal winter, but it can affect the atmospheric circulation and constituent distributions until the next autumn (McPhaden et al., 2006). It is well-known that strong ENSO events have a significant influence on tropical upwelling and STE. This change can impact the distribution of the composition and structure of the UTLS region. In the UTLS region, the tropopause responds to the annual and interannual variability associated with ENSO (Trenberth, 1990) and QBO (Baldwin et al., 2001). Several studies have been focused on the effects of the different impacts of El Niño on tropopause and lower stratosphere (Hu and Pan, 2009; Zubiaurre and Calvo, 2012; Xie et al., 2012). In the present study, we have investigated the changes associated with strong ENSO events with the anticyclone circulation and tropical upwelling during July and August. Therefore, we have also separated the GPH for the strongest El Niño (1958, 1966, 1973, 1983, 1988, 1992, 1998, and 2015) and La Niña (1974, 1976, 1989, 1999, 2000, 2008, and 2011) years to verify the change in the circulation pattern of the anticyclone. For this, we have chosen July and August GPH data at 100hPa as shown in Figure 8. The red and blue colors indicate the composite of the La Niña and El Niño circulation. During the La Niño, the anticyclone circulation is stronger and extends over the El Niña at 100 hPa as shown in the

Figure 8a. On the eastern and southern sides of the anticyclone, the expansion is more during the La Niña years. The warm temperature with strong westerlies in the latitude band of 43$^{o}$N-55$^{o}$N is observed during La Niño as shown in Figure 8b (Lau et al., 2018). The cooling impact is significant over the Tibetan Plateau during La Niña events compared to El Niño events. Significant cooling is observed over the Tibetan Plateau and distributes towards tropical latitudes between 600-100 hPa. The zonal wind shows a convergence of easterly winds over the Tibetan Plateau from the mid to the upper tropospheric region. On the right side of the Tibetan Plateau there exist strong westerly winds from the surface to the tropopause altitudes with strong warming. The meridional cross-section of temperature and the zonal wind difference between La Niña and El Niño is shown in Figure 8c. Significant cooling is observed during La Niña in the longitude band of 80$^{o}$E-100$^{o}$E with strong easterlies from the surface to the tropopause. From this analysis, it is clear that the Indian summer monsoon variability has a significant impact on ASMA, and it is necessary to consider the different phases of monsoon while dealing with UTLS pollutants. In addition, we have investigated the zonal mean vertical cross-section in the longitude band of 50-60$^{o}$E, which represents the Iranian Mode. Figure S3 depicts the difference between active and break phases, strong and weak monsoon years, and La Niño and El Niño years along with the tropopause altitude. Significant warming is observed during La Niña years and strong monsoon years compared to the active phase of the Indian monsoon in the troposphere. Compared to the Tibetan mode, Iranian mode warming is less. The tropopause altitude is slightly higher during the active phase of the Indian monsoon, strong monsoon years and La Niña years. A moderate increase in tropopause from the equator to 40$^{o}$N is observed and decreases drastically afterward.

## 4. Summary and Conclusions

Several authors discussed the interannual and decadal variability of pollutants and tracers in the ASMA region from the model, observational and reanalysis data sets (Kunze et al., 2016; Santee et al., 2017; Yuan et al., 2019). In this present study, we have investigated the spatial variability, trends of the anticyclone and the influence of Indian monsoon activity i.e. active and break days, strong and weak monsoon years, and strong La Niña and El Niño years on ASMA using long-term reanalysis, satellite and observational data sets that were not investigated earlier. In this study, we have considered the GPH values from 16.75 km to 16.9 km, which represents the spatial structure of the anticyclone at 100 hPa. Our analysis shows that the spatial extent (magnitude) of the anticyclone structure is very large (strong) during July followed by August whereas it is very weak in June at 100 hPa. The bimodal distribution (Tibetan and Iranian modes) of the anticyclone is clearly observed during the month of July which is absent during other months (June and August). The anticyclone variability undergoes significant decadal variations from one decade to another. The edges of ASMA changes drastically compared to the core of the anticyclone. However, there are significant spatial differences in the structure of the anticyclone at 100 hPa. The anticyclone undergoes a decreasing trend on the northern side whereas an increasing trend on the western part. A significant increasing trend is observed in the spatially averaged zonal wind in four different sectors (Figure 5). The zonal wind anomalies show increasing trend in all the sectors at 100 hPa. The change is significant in the north-western and north-eastern sectors with a magnitude variability of 7.59 m/s from 1951-2016 whereas it is 5.44 m/s in the south-eastern and south-western sectors. The strength of the anticyclone increases with a rate of 0.157 m/s per year (10.36 m/s from 1951-2016) in the anticyclone region (Figure 5e). Yuan et al. (2019) also reported the increasing trend in the strength of the anticyclone by considering the MERRA 2 reanalysis data from 2001-2015.

Further, we have investigated the Indian monsoon influence on the anticyclone region. Our results reveal that the spatial extent of the anticyclone expands during the active phase of the Indian monsoon, the strong monsoon years and during strong La Niña years on the northern and eastern sides. A similar expansion of the anticyclone is noticed during strong monsoon years from MERRA2 data by Yuan et al. (2019). However, the ASMA boundaries are not always well defined in all the events. The zonal mean cross-section of temperature shows significant warming over the Tibetan Plateau and from the surface to 12 km during the active phase of the Indian monsoon, the strong monsoon years, and the strong La Niña years. Similarly, the rise of tropopause during the active phase of the Indian monsoon, the strong monsoon years and the strong La Niña years are noticed. Since the Tibetan Plateau acts as a strong heat source in summer with the strongest heating layer lying in the lower layers, the thermal adaptation results in a shallow and weak cyclonic circulation near the surface, and a deep and strong anti-cyclonic circulation above it. During summer, the Tibetan Plateau acts as a strong heat source, which influences the whole UTLS region. The warm ascending air above will pull the air from below; the surrounding air in the lower troposphere converges towards the Tibetan Plateau area and climbs up the heating sloping surfaces (Bergman et al., 2013; Garny and Randel, 2016). Significant warming is observed over the Tibetan Plateau, which represents the strong transport of pollutants into the tropopause during the active phase of the Indian monsoon, the strong monsoon years, and the strong La Niña years. Pan et al. (2016) reported the transport of carbon monoxide through the southern flank of the Tibetan Plateau from the model analysis. The above-mentioned results indicate that the high mountain regions play a significant role in elevated heat sources during the formation and maintenance of the anticyclones over Asia. It emphasizes the role of the thermal forcing of the Tibetan Plateau on the temporal and the spatial evolution of the South Asian High. Lau et al. (2018) showed that the transport of the dust and pollutants from the Himalayas-Gangetic Plain and the Sichuan Basin.

Overall, we demonstrate the ASMA variability during different phases of the Indian monsoon. The uplifting of boundary layer pollutants to the tropopause level occurs primarily on the eastern side of the anticyclone, centered near the southern flank of the Tibetan Plateau, north-eastern India, Nepal, and north of the Bay of Bengal. The variability of tropopause altitude and temperature, trace gases (Water Vapour (WV), Ozone ($O_3$), Carbon Monoxide (CO) and aerosols (Attenuated Scattering Ratio (ASR) shows distinct in picture in ASMA region. The ASMA itself is highly dynamical in nature and the confinement of tracers and aerosols results in changes in its chemistry and radiation (Basha et al., 2019) However, a more detailed and higher quality of the dataset is needed to further understand the effects of the Tibetan Plateau on the transport of different tracers and pollutants to the UTLS region (Ravindrababu et al., 2019).

*Data Availability***.** The NCEP/NCAR reanalysis data are available from NOAA website (https://www.esrl.noaa.gov/psd/data/gridded/data.ncep.reanalysis.pressure.html). The COSMIC and CHAMP data is available from COSMIC CDAAC website. IMD gridded precipitation data is available at National Climate data center Pune, India. All the data used in the present study is available freely from the respective websites.

*Authors'Contributions*. GB and MVR conceived and designed the scientific questions investigated in the study. GB performed the analysis and wrote the draft in close association with MVR. PK estimated the active and break spells of the Indian monsoon. All authors edited the paper.

*Competing Interests.* The authors declare that they have no competing financial interests.

*Acknowledgements*. We thank NCEP/NCAR reanalysis for providing reanalysis data. We thank CDAAC for production of COSMIC and CHAMP GPSRO data and IMD gridded precipitation data from National Climate data center Pune, India. This work was supported by National Atmospheric Research Laboratory, Department of Space, and India

## References


Anthes, R. A., Bernhardt, P. A., Chen, Y., Cucurull, L., Dymond,K. F., Ector, D., Healy, S. B., Ho, S.-H., Hunt, D. C., Kuo, Y.-H., Liu, H., Manning, K., McCormick, C., Meehan, T. K., Randel,W. J., Rocken, C., Schreiner,W. S., Sokolovskiy, S. V., Syndergaard, S., Thompson, D. C., Trenberth, K. E., Wee, T.-K., Yen, N. L., and Zeng, Z.: The COSMIC/Formosat/3 mission: Early results, B. Am. Meteorol. Soc., 89, 313–333, 2008.

Rao, D. N., Ratnam, M. V., Mehta, S., Nath, D., Ghouse Basha, S., Jagannadha Rao, V. V. M., Krishna Murthy, B. V., Tsuda, T., and Nakamura, K.: Validation of the COSMIC radio occultation data over Gadanki (13.48 N, 79.2 E): A tropical region, Terr. Atmos. Ocean. Sci., 20, 59–70, doi:10.3319/TAO.2008.01.23.01(F3C), 2009.

Baldwin, M. P., Gray, L. J., Dunkerton, T. J., Hamilton, K., Haynes, P. H., Randel, W. J., Holton, J. R., Alexander, M. J., Hirota, I., Horinouchi, T., Jones, D. B. A., Kinnersley, J. S., Marquardt, C., Sato, K., and Takahashi, M.: The quasi-biennial oscillation, Rev. Geophys., 39, 179–229, doi:10.1029/1999RG000073, 2001.

Basha, G., Kishore, P., Ratnam, M.V., Ouarda, T.B.M.J., Velicogna, I., and Tyler sutterly.: Vertical and latitudinal variation of the intertropical convergence zone derived using GPS radio occultation measurements, *Remote Sensing of Environment*, http://dx.doi.org/10.1016/j.rse.2015.03.024, 2015.

Basha, G. and Ratnam, M. V.: Moisture variability over Indian monsoon regions observed using high resolution radiosonde measurements, Atmos. Res., 132–133, 35–45, https://doi.org/10.1016/j.atmosres.2013.04.004, 2013.

Basha, G., Kishore, P., Ratnam, M. V., Jayaraman, A., Kouchak, A. A., and Taha, B.J. M.: Historical and projected surface temperature over India during the 20th and 21st century. *Scientific Reports*, 7(1), 2987. https://doi.org/10.1038/s41598-017-02130-3, 2017.

Basha, G., Ratnam, M. V., Kishore, P., Ravindrababu, S., and Velicogna, I.: Influence of Asian Summer Monsoon Anticyclone on the Trace gases and Aerosols over Indian region, Atmos. Chem. Phys. Discuss., https://doi.org/10.5194/acp-2019-743, in review, 2019.

Bergman, J. W., Fierli, F., Jensen, E. J., Honomichl, S., and Pan, L. L.: Boundary layer sources for the Asian anticyclone: Regional contributions to a vertical conduit, J. Geophys. Res., 118, 2560–2575, https://doi.org/10.1002/jgrd.50142, 2013.

Beyerle, G., Schmidt, T., Wickert, J., Heise, S., Rotacher, M., Koenig-Langlo, G., and Lauritsen, K. B.: Observations and simulations of receiver-induced refractivity biases in GPS radio occultation, J. Geophys. Res., 111, D12101, doi:10.1029/2005JD006673. 2006.

Bian, J., Pan, L. L., Paulik, L., Vömel, H., and Chen, H.: In situ water vapor and ozone measurements in Lhasa and Kunmin during the Asian summer monsoon, Geophys. Res. Lett., 39, L19808, doi:10.1029/2012GL052996, 2012.

Bromwich, D. H., Fogt, R. L., Hodges, K. I., and Walsh, J. E.: A tropospheric assessment of the ERA-40, NCEP, and JRA-25 global reanalyses in the polar regions, J. Geophys. Res.-Atmos., 112, D10111, doi:10.1029/2006JD007859, 2007.

Fadnavis, S., Schultz, M. G., Semeniuk, K., Mahajan, A. S., Pozzoli, L., Sonbawne, S., Ghude, S. D., Kiefer, M., and Eckert, E.: Trends in peroxyacetyl nitrate (PAN) in the upper troposphere and lower stratosphere over southern Asia during the summer monsoon season:regional impacts, Atmos. Chem. Phys., 14, 12 725–12 743, https://doi.org/10.5194/acp-14-12725-2014, 2014.

Garny, H. and Randel, W. J.: Dynamic variability of the Asian monsoon anticyclone observed in potential vorticity and correlations with 5 tracer distributions, J. Geophys. Res., 118, 13 421–13 433, https://doi.org/10.1002/2013JD020908, 2013.

Garny, H. and Randel, W. J.: Transport pathways from the Asian monsoon anticyclone to the stratosphere, Atmos. Chem. Phys., 16, 2703-2718, https://doi.org/10.5194/acp-16-2703-2016, 2016.

Glatthor, N., Höpfner, M., Stiller, G. P., von Clarmann, T., Funke, B., Lossow, S., Eckert, E., Grabowski, U., Kellmann, S., Linden, A., Walker, K. A., and Wiegele, A.: Seasonal and interannual variations in HCN amounts in the upper troposphere and lower stratosphere observed by MIPAS, Atmos. Chem. Phys., 15, 563–582, https://doi.org/10.5194/acp-15-563-2015, 2015.

Gottschaldt, K.-D., Schlager, H., Baumann, R., Cai, D. S., Eyring, V., Graf, P., Grewe, V., Jöckel, P., Jurkat-Witschas, T., Voigt, C., Zahn, A., and Ziereis, H.: Dynamics and composition of the Asian summer monsoon anticyclone, Atmos. Chem. Phys., 18, 5655-5675, https://doi.org/10.5194/acp-18-5655-2018, 2018.

Hossaini, R., Chipperfield, M., Montzka, M. P., Rap, S. A., Dhomse, S., and Feng, W.: Efficiency of short-lived halogens at influencing climate through depletion of stratopsheric ozone, Nature Geoscience, 8, 186–190, https://doi.org/10.1038/ngeo2363, 2015.

Hoskins, B. J., and Rodwell, M. J.: A model of the Asian summer monsoon, I: The global scale, J. Atmos. Sci., 52, 1329–1340, 1995.

Highwood, E. J. and Hoskins, B. J.: The tropical tropopause, Q. J. Roy. Meteor.Soc., 124, 1579–1604, 1998.

Houze, R. A., Wilton, D. C., and Smull, B. F.: Monsoon convection in the Himalayan region as seen by the TRMM 345 Precipitation Radar, Q. J. Roy. Meteor. Soc., 133, 1389-1411, 10.1002/qj.106, 2007.

Hu, Y. and Pan, L.: Arctic stratospheric winter warming forced by observed SSTs, Geophys. Res. Lett., 36, L11707, doi:10.1029/2009GL037832, 2009.

Kishore, P., Ratnam, M. V., Namboothiri, S., Velicogna, I., Basha, G., Jiang, J., Igarashi, K., Rao, S., and Sivakumar, V.: Global (50◦ S–50◦ N) distribution of water vapor observed by COSMIC GPS RO: Comparison with GPS radiosonde, NCEP, ERAInterim, and JRA-25 reanalysis data sets, J. Atmos. Sol.-Terr. Phy., 73, 1849–1860, doi:10.1016/j.jastp.2011.04.017, 2011.

Kishore, P., Jyothi, S., Basha, G., Rao, S.V.B., Rajeevan, M., Velicogna, I., and Sutterley, T.C.: Precipitation climatology over India: validation with observations and reanalysis datasets and spatial trends. ClimDyn 121. doi: 10.1007/s00382-015-2597-y, 2015.

Kishore, P., Basha, G., VenkatRatnam, M., Velicogna, I., Ouarda, T. B. M. J., and Narayana Rao, D.: Evaluating CMIP5 models using GPS radio occultation COSMIC temperature in UTLS region during 2006–2013: twenty-first century projection and trends, Clim. Dynam., 47, 3253–3270, https://doi.org/10.1007/s00382- 016-3024-8, 2016.

Kalnay, E., Kanamitsu, M., Kistler, R., Collins, W., Deaven, D., Gandin, L., Iredell, M., Saha, D., White, G., Woollen, J., Zhu, Y., Chelliah, M., Ebisuzaki, W., Higgins, W., Janowiak, J., Mo, K.C., Ropelewski, C., Wang, J., Leetma, A., Reynolds, R., and Dennis, J.: The NCEP/NCAR 40-years reanalysis project. Bull. Am. Meteorol. Soc. 77, 437–472. 1996.

Kursinski, E. R., Hajj, G. A., Schofield, J. T., Linfield, R. P., and Hardy, K. R.: Observing Earth's atmosphere with radio occultation measurements using the Global Positioning System, J. Geophys. Res.-Atmos., 102, 23429–23465, 1997.

Kunze, M., Braesicke, P., Langematz, U., and Stiller, G.: Interannual variability of the boreal summer tropical UTLS in observations and CCMVal-2 simulations, Atmos. Chem. Phys., 16, 8695-8714, https://doi.org/10.5194/acp-16-8695-2016, 2016.

Lau, W.K.M., Cheng, Y., and Li, Z.: Origin, maintenance and variability of the Asian Tropopause Aerosol Layer (ATAL): Roles of monsoon dynamics. Sci. Rep. 2018, 8, 3960.

McPhaden, M. J., Zebiak, S. E., and Glantz M. H. ENSO as an integrating concept in earth science, Science, 314, 1740–1745, 2006.

Medina, S., Houze, R. A., Kumar, A., and Niyogi, D.: Summer monsoon convection in the Himalayan region: terrain and land cover effects, Q. J. Roy. Meteor.Soc., 136, 593-616, 10.1002/qj.601, 2010.

Narendra Reddy, N., Venkat Ratnam, M., Basha, G., and Ravikiran, V.: Cloud vertical structure over a tropical station obtained using long-term high-resolution radiosonde measurements, Atmos. Chem. Phys., 18, 11709–11727, https://doi.org/10.5194/acp-18-11709-2018, 2018.

Pai, D.S., Sridhar, L., and Ramesh Kumar, M.R.: Active and break events of Indian summer monsoon during 1901-2014. ClimDyn 46, 3921– 3939. https://doi.org/10.1007/s00382-015-2813-9, 2016.

Pan, L. L., Honomichl, S. B., Kinnison, D. E., Abalos, M., Randel, W. J., Bergman, J. W., and Bian, J.: Transport of chemical tracers from the boundary layer to stratosphere associated with the dynamics of the Asian summer monsoon, J. Geophys. Res. Atmos., 121, 14159-14174, 10.1002/2016JD025616, 2016.

Park, M., Randel, W. J., Gettleman, A., Massie, S. T., and Jiang, J. H.: Transport above the Asian summer monsoon anticyclone inferred from Aura Microwave Limb Sounder tracers, J. Geophys. Res., 112, D16309, https://doi.org/10.1029/2006JD008294, 2007.

Rajeevan, M., Gadgil, S., and Bhate, J.: Active and break spells of the Indian summer monsoon, J. Earth Syst. Sci., 119, 229–247, doi:10.1007/s12040-010-0019-4, 2010.

Randel, W. J., and Park, M.: Deep convective influence on the Asian summer monsoon anticyclone and associated tracer variability observed with Atmospheric Infrared Sounder (AIRS), J. Geophys. Res., 111, D12314, https://doi.org/10.1029/2005JD006490, 2006

Rao, D. N., Ratnam, M. V., Mehta, S., Nath, D., Ghouse Basha, S., Jagannadha Rao, V. V. M., Krishna Murthy, B. V., Tsuda, T., and Nakamura, K.: Validation of the COSMIC radio occultation data over Gadanki (13.48 N, 79.2 E): A tropical region, Terr. Atmos. Ocean. Sci., 20, 59–70, doi:10.3319/TAO.2008.01.23.01(F3C), 2009.

Ratnam, M. V., Sunilkumar, S., Parameswaran, K., Murthy, B. K., Ramkumar, G., Rajeev, K., Basha, G., Babu, S. R., Muhsin, M., and Mishra, M. K.: Tropical tropopause dynamics (TTD) campaigns over Indian region: An overview, J. Atmos. Sol.-Terr. Phy., 121, 229–239, 2014

RavindraBabu, S., VenkatRatnam, M., Basha, G., Krishnamurthy, B. V., and Venkateswararao, B.: Effect of tropical cyclones on the tropical tropopause parameters observed using COSMIC GPS RO data, Atmos. Chem. Phys., 15, 10239–10249, doi:10.5194/acp-15-10239-2015, 2015.

Ravindrababu, S., Ratnam, M.V., Basha, G., Liou, Y.-A., Reddy, N.N.: Large Anomalies in the Tropical Upper Troposphere Lower Stratosphere (UTLS) Trace Gases Observed during the Extreme 2015–16 El Niño Event by Using Satellite Measurements. *Remote Sens.* 2019, *11*(6), 687; https://doi.org/10.3390/rs11060687, 2019.

Riese, M., Ploeger, F., Rap, A., Vogel, B., Konopka, P., Dameris, M., and Forster, P.: Impact of uncertainties in atmospheric mixing on simulated UTLS composition and related radiative effects, J. Geophys. Res., 117, D16305, https://doi.org/10.1029/2012JD017751, 2012.

Santee, M. L., Manney, G. L., Livesey, N. J., Schwartz, M. J., Neu, J. L., and Read, W. G.: A comprehensive overview of the climatological composition of the Asian summer monsoon anticyclone based on 10 years of Aura Microwave Limb Sounder measurements, J. Geophys. Res.-Atmos., 122, 5491– 5514, https://doi.org/10.1002/2016JD026408, 2017

Schreiner, W., Rocken, C., Sokolovskiy, S., Syndergaard, S., and Hunt, D.: Estimates of the precision of GPS radio occultations from the COSMIC/FORMOSAT-3 mission, Geophys. Res. Lett., 34, L04808, doi:10.1029/2006GL027557, 2007.

Sokolovskiy, S. V., Kuo, Y.-H., Rocken, C., Schreiner, W. S., Hunt, D., and Anthes, R. A.: Monitoring the atmospheric boundary layer by GPS radio occultation signals recorded in the open-loop mode, Geophys. Res. Lett., 33, L12813, doi:10.1029/2006GL025955, 2006.

Solomon, S., Rosenlof, K., Portmann, R., Daniel, J., Davis, S., Sanford, T., and Plattner, G.-K.: Contributions of stratospheric water vapor to 5 decadal changes in the rate of global warming, Science, 327, 1219–1223, https://doi.org/10.1126/science.1182488, 2010

Tissier, A.-S., and Legras, B.: Convective sources of trajectories traversing the tropical tropopause layer, Atmos. Chem. Phys., 16, 3383–3398, doi:10.5194/acp-16-3383-2016, 2016.

Trenberth, K. E.: Recent observed interdecadal climate changes in the Northern Hemisphere, B. Am. Meteorol. Soc., 71, 988–993, doi:10.1175/1520-0477(1990)0712.0.CO;2, 1990.

Vernier, J. P., Fairlie, T. D., Natarajan, M.,Wienhold, F. G., Bian, J., Martinsson, B. G., Crumeyrolle, S., Thomason, L.W., and Bedka, K. M.: Increase in upper tropospheric and lower stratospheric aerosol levels and its potential connection with Asian pollution, J. Geophys. Res., https://doi.org/10.1002/2014JD022372, 2015

Vogel, B., Günther, G., Müller, R., Grooß, J.-U., Afchine, A., Bozem, H., Hoor, P., Krämer, M., Müller, S., Riese, M., Rolf, C., Spelten, N., Stiller, G. P., Ungermann, J., and Zahn, A.: Long-range transport pathways of tropospheric source gases originating in Asia into the northern lower stratosphere during the Asian monsoon season 2012, Atmos. Chem. Phys., 16, 15 301–15 325, https://doi.org/10.5194/acp-16-15301-2016, 2016.

Vogel, B., Günther, G., Müller, R., Grooß, J.-U., and Riese, M.: Impact of different Asian source regions on the composition of the Asian monsoon anticyclone and of the extratropical lowermost stratosphere, Atmos. Chem. Phys., 15, 13 699–13 716, https://doi.org/10.5194/acp15-13699-2015, http://www.atmos-chem-phys.net/15/13699/2015/, 2015.

Wickert, J., Reigber, C., Beyerle, G., Konig, R., Marquardt, C., Schmidt, T., Grunwaldt, L., Galas, R., Meehan, T. K., Melbourne, W. G., and Hocke, K.: Atmosphere sounding by GPS radio occultation: First results from CHAMP, Geophys. Res. Lett., 28, 3263–3266, 2001.

Xie, F., Li, J., Tian, W., Feng, J., and Huo, Y.: Signals of El Niño Modoki in the tropical tropopause layer and stratosphere, Atmos. Chem. Phys., 12, 5259-5273, https://doi.org/10.5194/acp-12-5259-2012, 2012.

Yan, R.-C., Bian, J.-C., and Fan, Q.-J.: The impact of the South Asia high bimodality on the chemical composition of the upper troposphere and lower stratosphere, Atmos. Ocean. Sci. Lett., 4, 229–234, 2011.

Yuan, C., Lau, W. K. M., Li, Z., and Cribb, M.: Relationship between Asian monsoon strength and transport of surface aerosols to the Asian Tropopause Aerosol Layer (ATAL): interannual variability and decadal changes, Atmos. Chem. Phys., 19, 1901-1913, https://doi.org/10.5194/acp-19-1901-2019, 2019.

Zhang, Q., Wu, G., and Qian, Y.: The Bimodality of the 100 hPa South Asia High and its Relationship to the Climate Anomaly over East Asia in summer, J. Meteorol. Soc. Jpn., 80, 733–744, 2002.

Zubiaurre, I., and Calvo, N.: The El Nino–Southern Oscillation (ENSO) Modoki signal in the stratosphere, J. Geophys. Res., 117, D04104, doi:10.1029/2011JD016690, 2012.

**Figures**

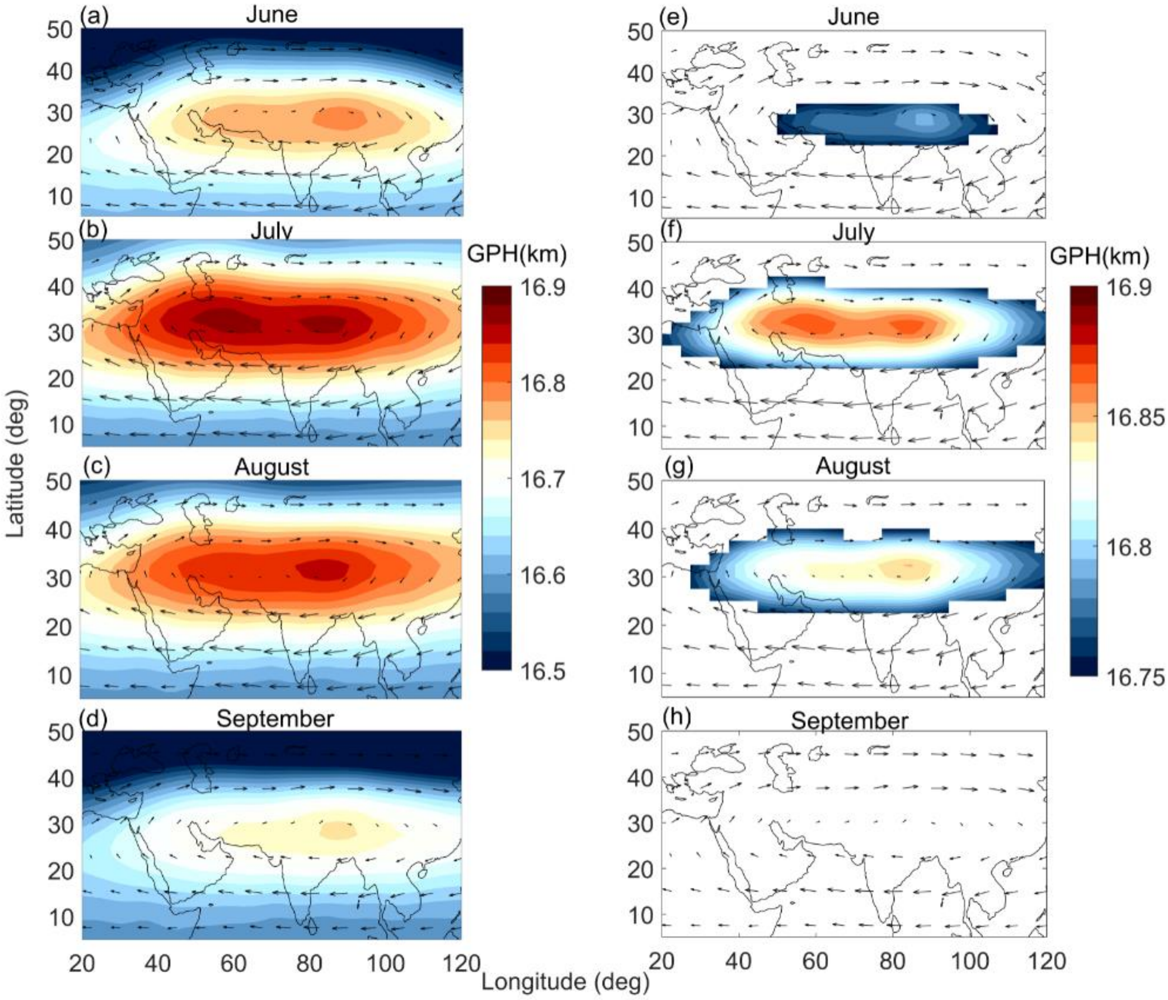


Figure 1. Spatial distribution of Geopotential Height (GPH) and wind vectors at 100 hPa during (a) June, (b), July, (c) August and (d) September from NCEP reanalysis data averaged from the year 1951-2016. The core of the anticyclone region was chosen based on the GPH values ranging from 16.75 to 16.9 km. The spatial extent and magnitude of the anticyclone after applying the GPH criteria for (e) June, (f) July, (g) August and (h), September.

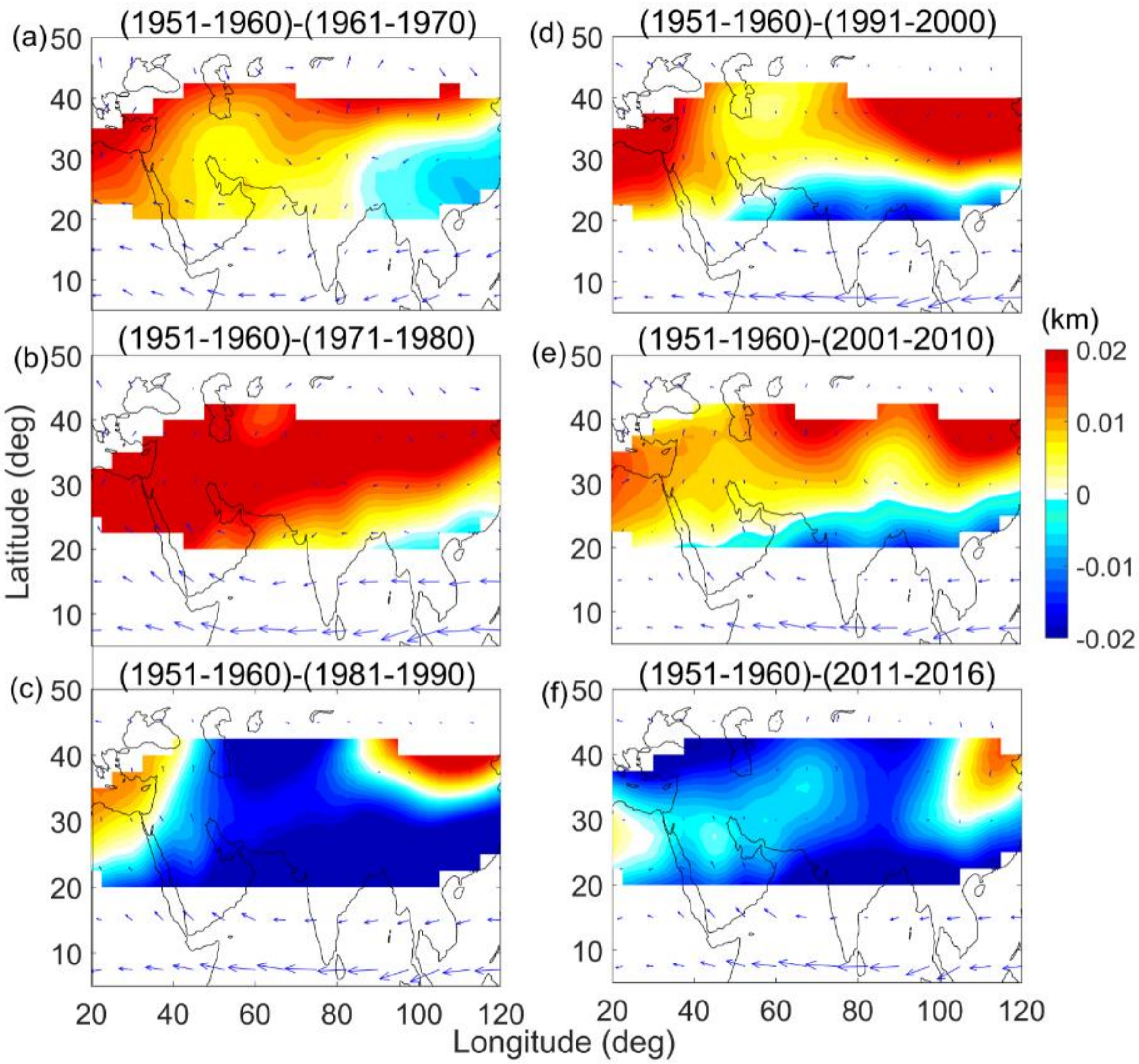


Figure 2. Decadal variation of anticyclone obtained from GPH and wind vectors with reference to 1951-1960 period.

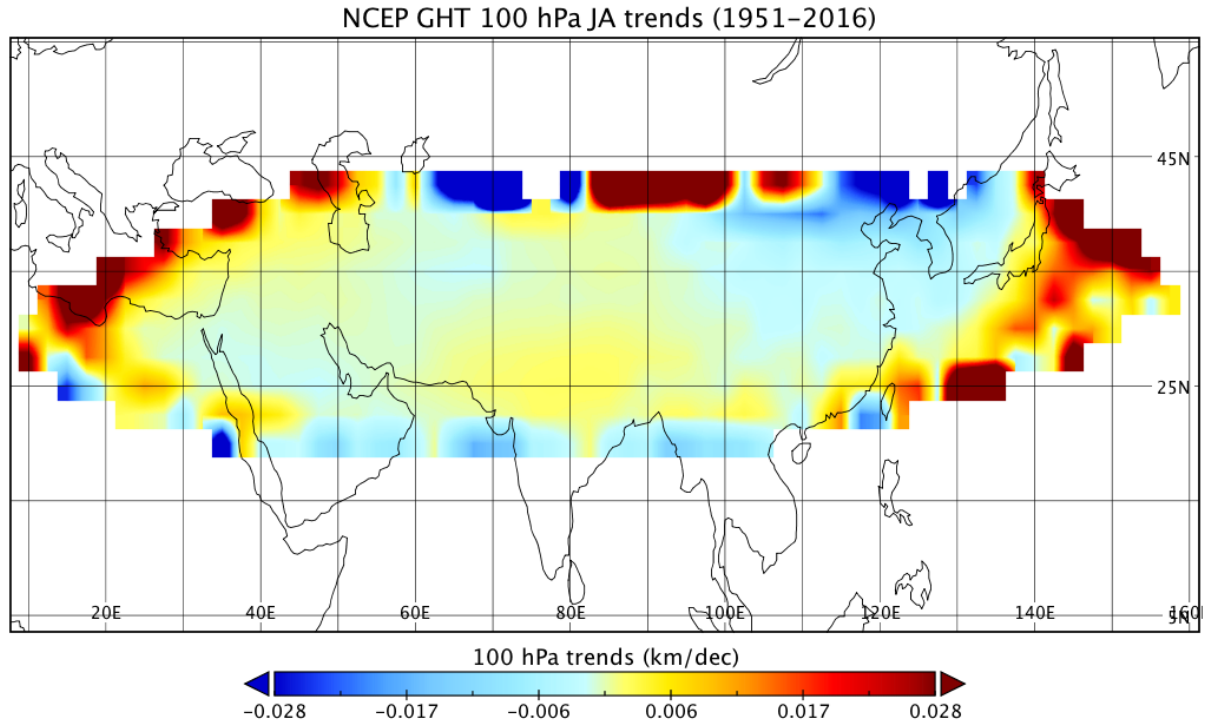


Figure 3. Spatial trend analysis obtained using robust regression analysis at 95% confidence interval.

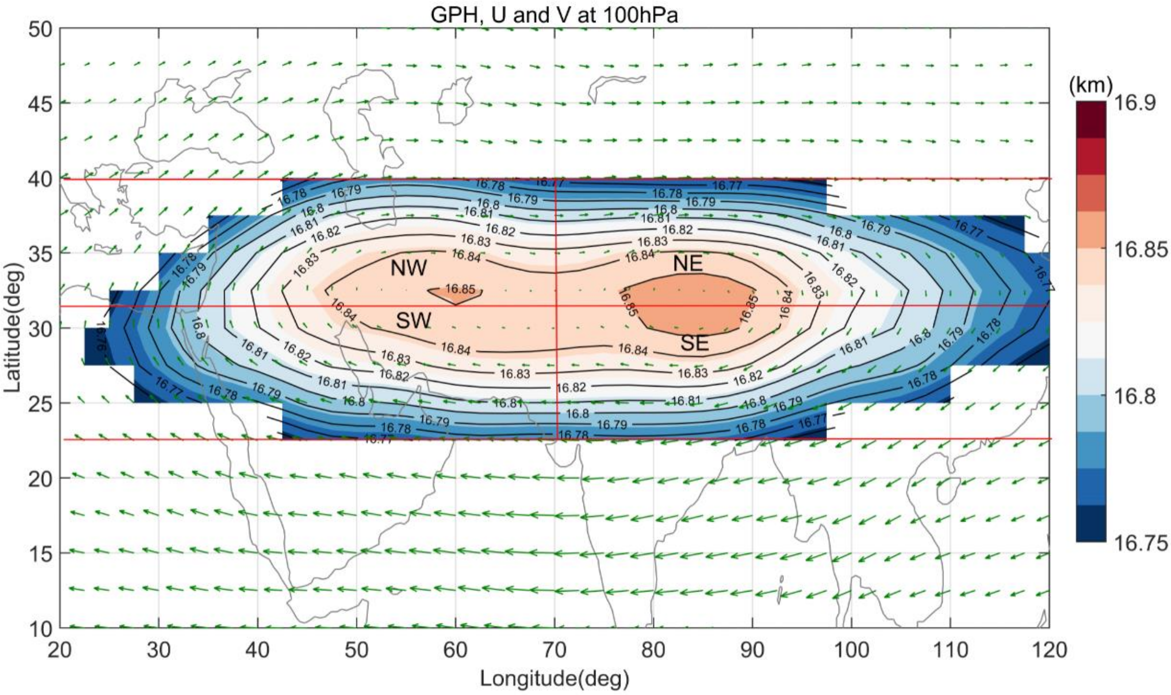


Figure 4.The climatological distribution of GPH (16.75 to 16.9 km) and wind vectors averaged during July and August from NCEP reanalysis data along with contour lines at 100 hPa from 1951-2016. The anticyclone region is further divided in to 4 sectors based on peak values of GPH. The GPH values peak centres at 32.5$^{o}$N in latitude and 70$^{o}$E in longitude. The sectors are further divided in to South-East (SE) (22.5$^{o}$N-32.5$^{o}$N), North-East (NE) (32.5$^{o}$N-40$^{o}$N) in longitude band 70$^{o}$E-120$^{o}$E, South-West (SW) (22.5$^{o}$N-32.5$^{o}$N), and North-West (NW) (32.5$^{o}$N-40$^{o}$N) at 20$^{o}$E-70$^{o}$E longitude range.

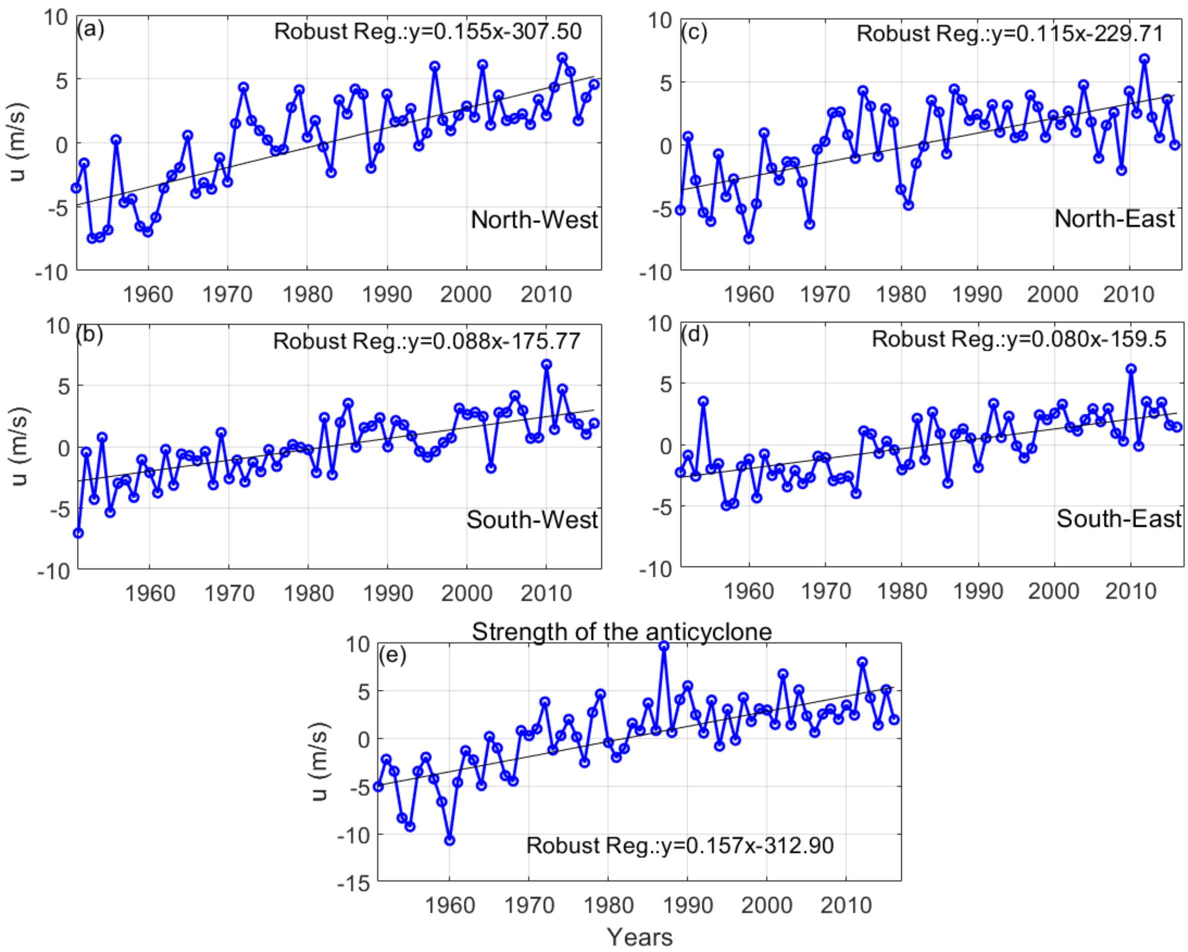


Figure 5.Time series of zonal wind anomalies estimated for (a) North-West, (b) South-West, (c) North-East and (d) South-East sectors of ASMA. The trend analysis was performed at 95% confidence interval by using robust regression analysis. (e) The strength of the anticyclone was estimated from the zonal wind difference between (30$^{o}$N-40$^{o}$N)-(10$^{o}$N-20$^{o}$N) in the longitude band of 50$^{o}$E-90$^{o}$E.

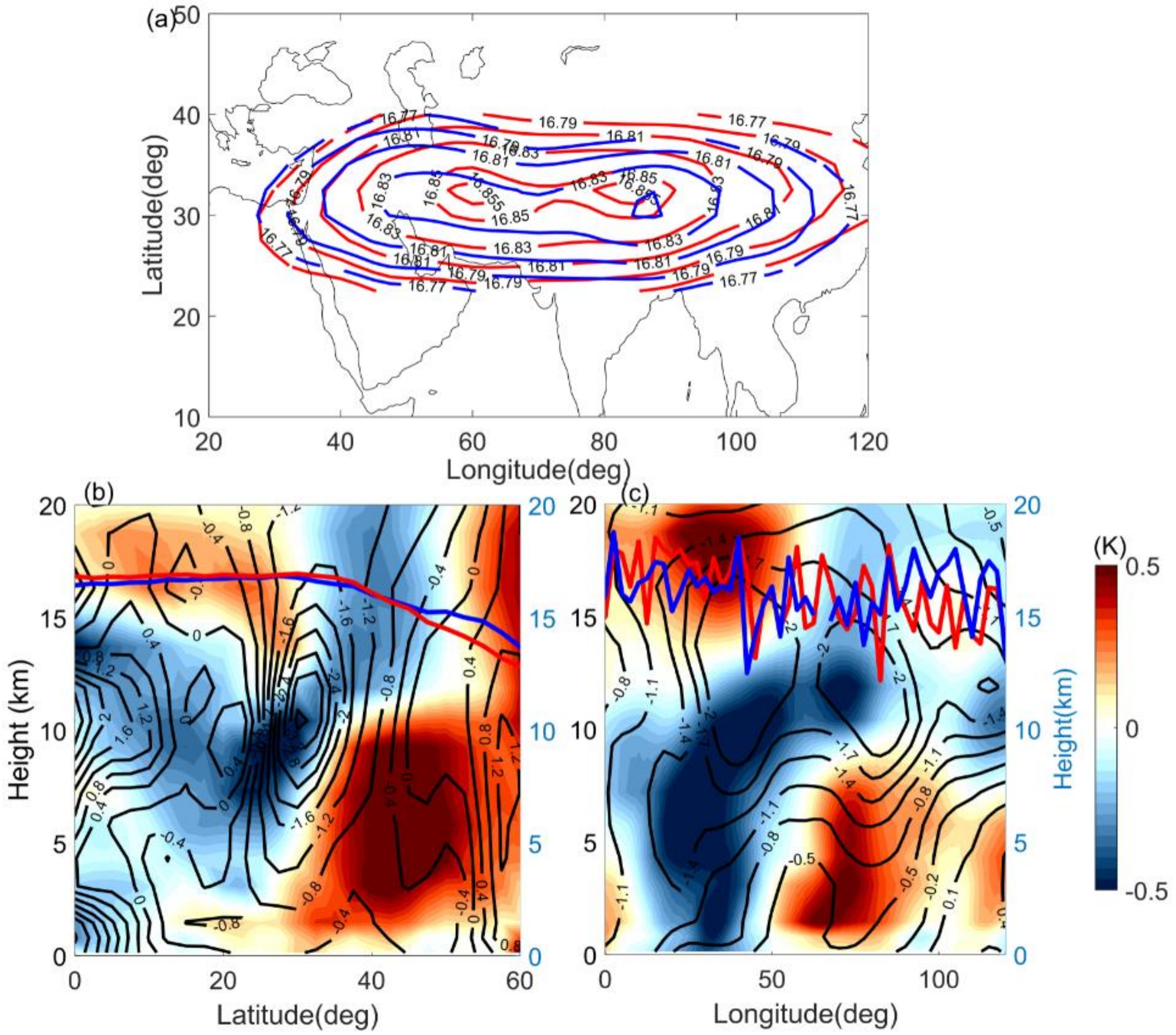


Figure 6. (a) ASMA variability during active and break phases of Indian monsoon obtained from GPH at 100 hPa. Red line indicates the active and blue line for break phase of Indian monsoon. (b) Latitude-altitude cross-section of temperature (colour shaded, K) and zonal wind anomalies (contour lines, m/s) which are estimated from difference between active and break phases of Indian Monsoon in the longitude band of 80$^{o}$E-90$^{o}$E. (c) Longitude-altitude cross-section of temperature and wind anomalies averaged between 30$^{o}$N-40$^{o}$N. The red and blue lines in Figure 6b & 6c denotes the tropopause altitude during active and break spells of Indian monsoon estimated using GNSS RO data, respectively.

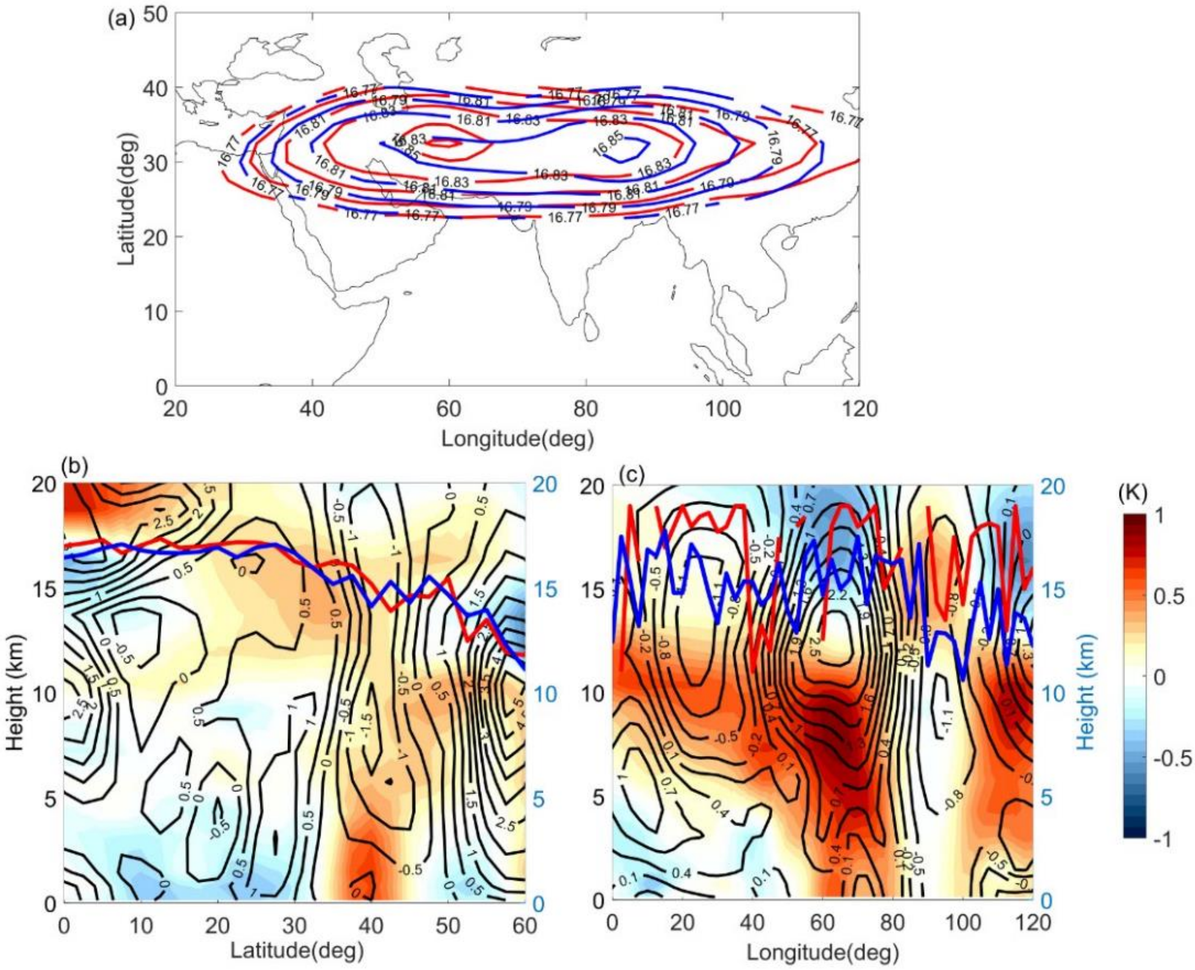


Figure 7. (a) ASMA variability obtained from GPH at 100hPa during strong and weak monsoon years calculated based on high resolution rainfall data in band of 5°N-30°N, 70°N-95°E grid. Red line indicates the strong and blue line for weak monsoon years. (b) Latitude-altitude cross-section of temperature (colour shaded, K) and zonal wind anomalies (contour lines, m/s) which are estimated from difference between strong and weak monsoon years in the longitude band of 80$^{o}$E-90$^{o}$E. (c) Longitude-altitude cross-section of temperature and wind anomalies averaged between 30$^{o}$N-40$^{o}$N. Red and blue lines in Figure 7b & 7c denote the tropopause altitude during strong and weak monsoon years estimated using GNSS RO data, respectively.

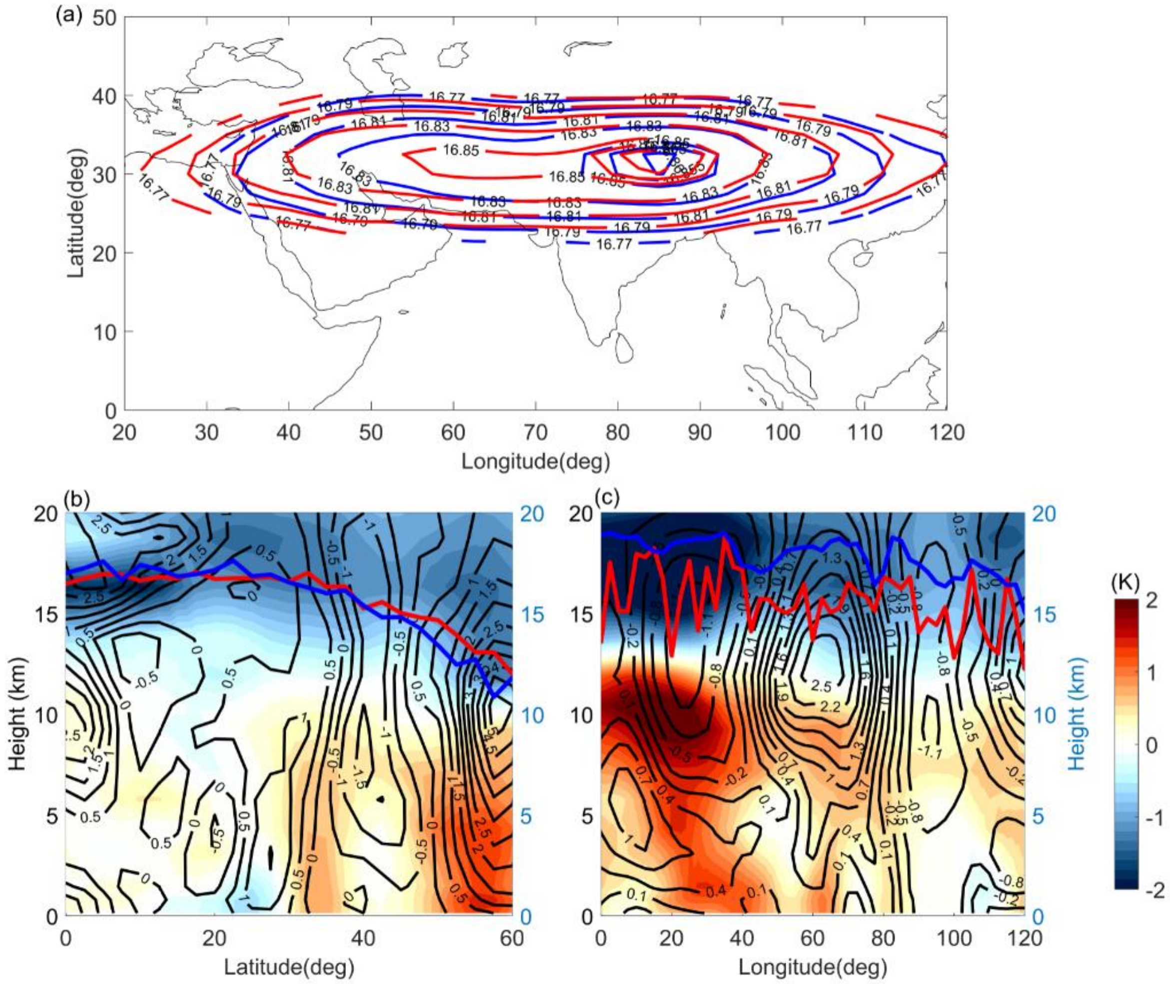


Figure 8. (a) ASMA variability obtained from GPH at 100 hPa during strong La Niño and El Niño years. Red and blue lines indicate the La Niño and El Niño years. (b) Latitude-altitude cross-section of temperature (colour shaded, K) and zonal wind anomalies (contour lines, m/s) which are estimated from difference between La Niño and El Niño years in the longitude band of 80$^o$E-90$^o$E. (c) Longitude-altitude cross-section of temperature and zonal wind anomalies averaged between 30$^o$N-40$^o$N. The red and blue lines in Figure 8b & 8c denote the tropopause altitude during La Niño and El Niño years estimated from GNSS RO data, respectively.